Effect of Pt nanoparticle decoration on the H2 storage performance of plasma-derived nanoporous graphene

Document Version
Final published version

Research Article

Effect of Pt nanoparticle decoration on the H_2 storage performance of plasma-derived nanoporous graphene

Nikolaos Kostoglou [a, *], Chi-Wei Liao [b], Cheng-Yu Wang [c, **], Junko N. Kondo [d], Christos Tampaxis [e], Theodore Steriotis [e], Konstantinos Giannakopoulos [e], Athanassios G. Kontos [f, e], Steve Hinder [g], Mark Baker [g], Etienne Bousser [h], Allan Matthews [h], Claus Rebholz [a, h, i], Christian Mitterer [a]

[a] Department of Materials Science, Montanuniversität Leoben, 8700, Leoben, Austria
[b] Department of Materials Science, Feng Chia University, Taichung, 40724, Taiwan
[c] Department of Materials Science and Engineering, National Chiao Tung University, Hsinchu, 30010, Taiwan
[d] Institute of Innovative Research, Tokyo Institute of Technology, Yokohama, 226-8503, Japan
[e] Institute of Nanoscience and Nanotechnology, National Center for Scientific Research Demokritos, 15341, Athens, Greece
[f] School of Applied Mathematical and Physical Sciences, National Technical University of Athens, 15780, Athens, Greece
[g] Department of Mechanical Engineering Sciences, University of Surrey, GU27XH, Guildford, UK
[h] Department of Materials, University of Manchester, Manchester, M13BB, UK
[i] Department of Mechanical and Manufacturing Engineering, University of Cyprus, 1678, Nicosia, Cyprus

ARTICLE INFO

ABSTRACT

A nanoporous and large surface area (~800 m^2/g) graphene-based material was produced by plasma treatment of natural flake graphite and was subsequently surface decorated with platinum (Pt) nano-sized particles via thermal reduction of a Pt precursor (chloroplatinic acid). The carbon-metal nano-composite showed a ~2 wt% loading of well-dispersed Pt nanoparticles (<2 nm) across its porous gra-phene surface, while neither a significant surface chemistry alteration nor a pore structure degradation was observed due to the Pt decoration procedure. The presence of Pt seems to slightly promote the hydrogen sorption behavior at room temperature with respect to the pure graphene, thus implying the rise of "weak" chemisorption phenomena, including a potential hydrogen "spillover" effect. The findings of this experimental study provide insights for the development of novel graphene-based nano-composites for hydrogen storage applications at ambient conditions.

1. Introduction

Considering the increased emission of greenhouse gases and the limited availability of fossil fuels worldwide, people are seeking for clean, reliable and renewable energy technologies [1]. The volatile nature of green energy sources, such as solar or wind power plants, makes it difficult to satisfy the base load requirement. Thus, the combination of green energy conversion and storage becomes an important task. Hydrogen (H_2) is a strong candidate as a renewable and carbon-free energy carrier because of its high gravimetric en-ergy density, highly efficient electrochemical combination with oxygen in fuel cells and environmental friendliness with water as the only "product" after utilization [2–4].

However, the fundamental obstacle for the transition to a H_2-fueled society is the efficient H_2 storage [5,6]. H_2 storage materials which are based on physisorption (sorbents) and chemisorption (hydrides) phenomena can only meet the goals set up by the U.S. Department of Energy for transportation purposes (i.e. reversible capacity of 4.5 wt% by 2020 with ultimate target of 6.5 wt%) [7] at temperature and/or pressure conditions which lead to substantial energy losses and moreover are highly inconvenient for practical applications. For example, porous carbon-based materials with high specific surface area have been proposed for H_2 adsorption, including activated carbons [8–10], carbon nanotubes [11–13],

* Corresponding author.
** Corresponding author.
E-mail addresses: nikolaos.kostoglou@unileoben.ac.at (N. Kostoglou), ChengYuWang@nctu.edu.tw (C.-Y. Wang).

templated carbons [14] and more recently graphene-based nanostructures [15–17]. The H_2 adsorption capacity is, in most cases, proportional to the specific surface area, as shown by the so-called "Chahine" rule [11,18], and hence significant H_2 uptakes can be reached with high surface area nanoporous carbons. Moreover, sub-nanometer pores act as "strong" adsorption sites due to overlapping potential fields from opposite pore walls and thus such pores could further improve the H_2 storage behavior of a sorbent material [19]. Nonetheless, a cryogenic environment is necessary to reach a high H_2 uptake due to the low heat of adsorption (<10 kJ/mol), which is the major drawback, since the additional auxiliary equipment needed for cooling purposes significantly adds extra weight and a severe energy penalty to the H_2 storage system [20,21].

As physisorption leads to a low H_2 uptake at room temperature, the addition of platinum group metals (PGM) to carbon-based materials has been suggested as a means to increase the solid-H_2 interactions and achieve a higher heat of adsorption. PGM decoration can initiate the so called H_2 "spillover" effect, which refers to the dissociation of molecular H_2 by well-dispersed catalysts, followed by migration of hydrogen atoms from the catalysts to the sorbent and diffusion onto adjacent surface sites [22,23]. Hence, this mechanism has been proposed as a method to store H_2 at ambient temperatures because of potential "weak" chemisorption effects [24]. As several carbon-based materials have a quite active surface [25], a series of materials with improved room temperature H_2 adsorption behavior via spillover have been reported [23,26–28]. For instance, Pd-doped nanoporous carbons showed enhanced H_2 uptake at 298 K and 20 bar, compared to their undoped counterparts, especially with the assistance of oxygen surface groups [29,30]. Moreover, acid-treated carbon nanotubes doped with Pt doubled their H_2 uptake at 70 bar and room temperature [31]. Pd nanoparticles on graphene sheets mixed with activated carbon demonstrated a H_2 uptake higher than that of neat graphene or activated carbon at room temperature along with an enhanced heat of adsorption value [32]. H_2 spillover has also been observed in other nanocomposite materials systems such as Pt-loaded graphene oxide/metal organic framework composites [33,34]. Even though there are some examples of enhanced H_2 storage at ambient temperatures, discrepancies were found in some catalyst-carbon nanocomposites. For instance, well-dispersed Pt nanoparticles on activated carbon facilitates H_2 storage via spillover [35], however, in another similar system the additional deadweight from PGM decreased the total uptake [36].

Spectroscopic observations of atomic hydrogen on sorbents in the form of C—H by infrared radiation [37–39] and neutron scattering [40–42] provided strong evidences of H_2 adsorption on carbon via spillover and thus revealed H_2 spillover feasibility. Hence, it is a matter of effective material design for a successful H_2 spillover demonstration. To deal with the irreproducibility in H_2 spillover, several possible factors have been proposed. For catalysts, it has been concluded that a proper nanoparticle size in the range of few nanometers and a homogeneous dispersion should be reached in order to shorten the diffusion path for atomic hydrogen [43–46], while uneven dispersion or large PGM particles might not lead to a measurable H_2 spillover effect [47]. In this context, it has been reported that surface modifications, including heteroatom substitution [48,49] and oxygen functionalization [50], could lead to a good transition metal dispersion, since electrostatic attractions between hydroxyl surface groups and chloroplatinic acid may anchor the metal cations.

Atomic hydrogen may encounter a huge energy barrier between catalysts and supports and also between adjacent adsorption sites on sorbents [46,51,52]. Several possible surface modifications have been proposed to this end. For example, it has been calculated that

the atomic hydrogen migration energy barrier might be reduced with possible defects [31,53,54], curvatures of fullerene [55] or reducible surfaces [56]. In addition, some functional groups or surface decorations show effectiveness in the activation energy reduction. In theoretical simulations a graphene surface decorated with boron reduced the energy barrier for atomic hydrogen diffusion [57]. Several experimental studies have also demonstrated that oxygen-based functional groups (hydroxyls, carboxyls, etc.) on carbon surfaces could facilitate the H_2 spillover effect, as long as they do not exceed a threshold [29,30,58–61]. To sum up, the main obstacle in H_2 spillover is the high activation energy and long diffusion path for hydrogen "hopping" on the sorbent surface [25].

To this end, a PGM-decorated carbon-based material should be developed with a good catalyst dispersion, shortened atomic hydrogen diffusion length, surface functionalization for activation energy reduction and reasonable surface area reduction due to the loaded-PGM dead weight. In this respect, a platinum (Pt)-decorated nanoporous few-layer graphene was synthesized with the aim to address all these challenges. The neat graphene-based material was produced in a powder form by plasma-induced exfoliation of natural flake graphite to achieve a short graphene length with surface functional groups as well as possible manipulated defects. The plasma modifies the graphitic surface in a physical (i.e. ablation) and/or chemical (i.e. functionalization) manner, depending on the working gas and the operating power of the plasma reactor [62,63]. The plasma-derived graphene powder was decorated with Pt nanoparticles via thermal reduction under a H_2 flow using a Pt precursor. Both neat and Pt-decorated graphene samples were studied for their nanostructure, chemical composition, morphology and nanoporosity using a broad variety of characterization methods, including X-ray diffraction (XRD), Raman spectroscopy, X-ray photoelectron spectroscopy (XPS), thermal gravimetric analysis (TGA) combined with differential scanning calorimetry (DSC), scanning electron microscopy (SEM) combined with energy dispersive X-ray spectroscopy (EDS), transmission electron microscopy (TEM) and nitrogen (N_2) adsorption/desorption measurements at 77 K. The H_2 storage properties, such as gravimetric H_2 uptake, reversibility, cyclic stability and kinetics, were evaluated using high-pressure (0–20 bar) H_2 adsorption/desorption measurements at cryogenic (i.e. 77 K) and room (i.e. 298 K) temperature.

The current work focuses on the development of a graphene-based H_2 storage material operating in ambient conditions and sheds light on the respective H_2 storage mechanisms involved in such PGM-carbon nanocomposite structures. Despite the fact that a plethora of carbon-metal systems have been investigated for H_2 spillover in the past, no great emphasis has been given on the H_2 sorption reversibility, cyclic stability and kinetics, as done in the current study. Most of the previous H_2 spillover studies focused only on the improvement of the H_2 sorption capacity without providing further information about the abovementioned H_2 storage properties and even sometimes presenting only a single H_2 sorption isotherm at 298 K (i.e. no desorption branch, no additional cycles and no kinetics curves).

2. Materials and methods

2.1. Plasma-derived graphene

The nanoporous few-layer graphene powder (denoted hereafter as FLG) was produced by adopting a plasma-induced exfoliation method of natural graphite using a custom-made multi-electrode dielectric barrier discharge plasma reactor, as described in a previous study [16]. Briefly, a flake graphite powder (Asbury Carbons, UK) was exposed to argon and oxygen plasmas using 0.01 mbar

pressure and 600 sccm flow for 1.5 h towards exfoliation. The resulting FLG is comprised of defective few-layer graphene stacks with less than 2 μm diameter, less than 3 nm thickness, up to ~800 m^2/g specific surface area and ~5.5 at% oxygen content.

2.2. Pt-decorated graphene

The methodology for decorating carbon surfaces with Pt nanoparticles was adopted from Wang and co-workers [64]. In a typical synthesis, 200 mg of the FLG powder was pre-treated at 250 °C for 12 h under an Ar flow of 100 sccm. About 180 mg of the FLG powder, left upon pre-treatment, was dispersed in 50 mL of acetone (C$_3$H$_6$O) under magnetic stirring. In a next step, 10 mg of chloroplatinic acid (H$_2$PtCl$_6$·6H$_2$O; Alfa Aesar) was dissolved completely in 4 mL of C$_3$H$_6$O via ultra-sonication and added dropwise with a rate of 20 s/drop into the abovementioned FLG-suspended solution. The mixture solution of FLG and Pt precursor was ultra-sonicated for 1 h, followed by magnetic stirring for 1 h. About 190 mg of black powder of PtCl$_4^{2-}$/FLG was collected upon C$_3$H$_6$O evaporation at 60 °C for 12 h and was then loaded in a tube furnace for a 3-time degassing process under Ar/vacuum reversibly. The sample was pre-heated under an Ar flow of 100 sccm at 80 °C for 2 h for possible residual solvent removal and then switched to a H$_2$ flow of 100 sccm and raised to 300 °C for 2 h with a heating rate of 1 °C/min. The final product (denoted hereafter as Pt-FLG) of 165 mg was obtained upon cooling to room temperature under an Ar flow of 100 sccm. Fig. 1 demonstrates a simplified schematic of the described synthesis procedures, including the plasma treatment of natural graphite (see section 2.1) and the metal decoration of the plasma-derived graphene using a Pt precursor.

2.3. Characterization methods

XRD measurements were performed using a Bruker-AXS D8 Advance diffractometer equipped with Cu Kα radiation (λ ~0.154 nm) at 40 kV voltage and 40 mA current. The X-ray diffractograms were recorded in the Bragg-Brentano geometry using a continuous scan speed mode in the diffraction angle range 2θ = 10–60°, a 0.01° step width and a 0.5°/min scan speed. The domain and crystal sizes of carbon and Pt, respectively, were estimated from the Full Width at Half Maximum (FWHM) of the carbon (002) and Pt (111) reflections, respectively, using the Scherrer equation.

Micro-Raman spectroscopic studies were performed using an inVia Reflex Renishaw spectrometer and a solid-state laser emitting at 514.5 nm for excitation. The laser beam was focused on spots of 4.5 μm in diameter with an objective lens having × 20 magnification and 0.14 numerical aperture. The corresponding focal area (20 μm^2) averages well the Raman signal, as verified by measuring very similar spectra from different areas. After performing initial test measurements, a power density of 0.02 mW/μm^2 was defined as entirely safe for examining the samples without affecting their Raman signal by laser heating. The recorded Raman spectra were peak fitted with mixed Lorentzian-Gaussian components in order to achieve a high-quality quantitative analysis.

XPS analysis was carried out by a Thermo Scientific Theta Probe spectrometer equipped with a monochromated Al Kα radiation source (hν = 1486.6 eV) using an X-ray spot of ~400 μm in radius. Survey spectra were acquired using a pass energy of 300 eV, while a high-resolution core level spectrum for the C1s component was acquired with a pass energy of 50 eV. All spectra were charge referenced against the C1s peak at 284.5 eV (sp^2 hybridized carbon) to correct for charging effects during acquisition. Quantitative chemical compositions were determined from the high-resolution core level spectra, using instrument modified Wagner sensitivity factors, following the removal of a non-linear Shirley background.

TGA and DSC curves were simultaneously recorded by a SETARAM SETSYS Evolution 18 thermal analyzer in the temperature range 25–1300 °C using a heating rate of 10 K/min under a HC-free synthetic air flow of 16 mL/min. Samples of ~10 mg were placed in alumina crucibles, while buoyancy effects were taken into account by performing a blank experiment. Prior to thermal analysis, purging was applied to remove any residual contaminants from the furnace.
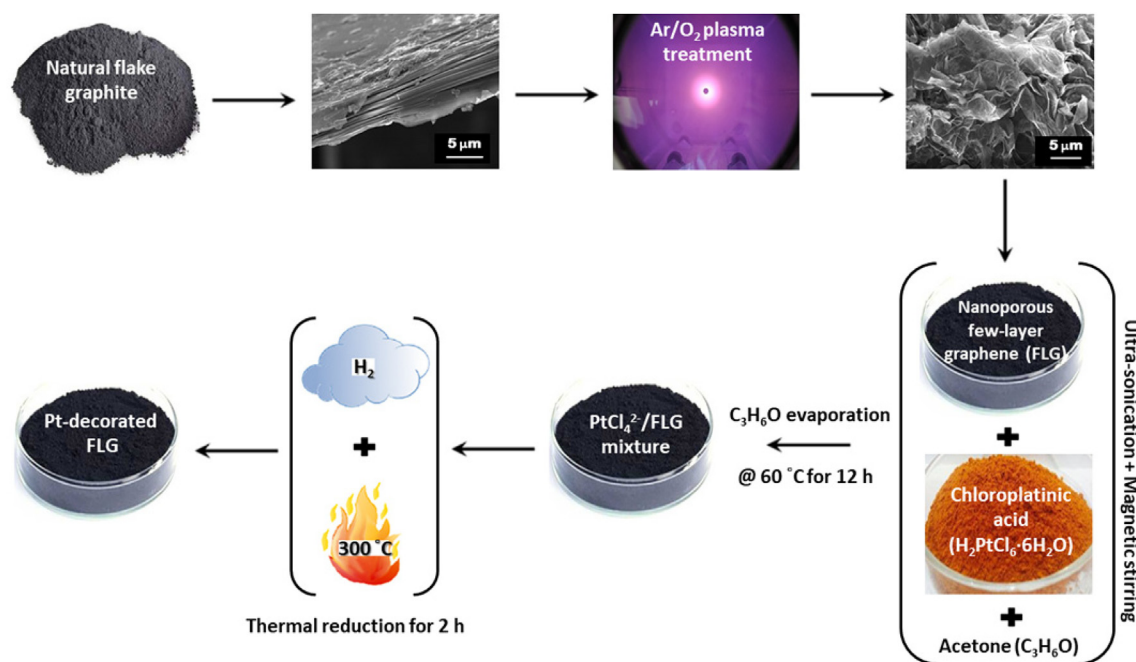

Fig. 1. Main synthesis steps of the nanoporous FLG material via plasma processing of natural flake graphite (on the top) and the Pt-FLG nanocomposite via thermal reduction of H$_2$PtCl$_6$ (on the bottom). (A colour version of this figure can be viewed online.)

Secondary electron images using an InLens detector and Back-Scattered Electron (BSE) images were acquired at 4 kV using a Zeiss Merlin ultra-high-resolution field emission gun (FEG) scanning electron microscope equipped with a Gemini II column. The elemental maps were collected with two parallel integrated Oxford Instruments XMAX 150 mm^2 EDS detectors using the same 4 kV acceleration voltage. The acquired data were analyzed using Oxford Instruments AZtec software.

TEM studies were carried out by employing a Philips CM-20 transmission electron microscope with high-resolution capabilities equipped with a LaB$_6$ filament and operated at 200 kV acceleration voltage. The powders were first ultra-sonicated in ethanol and then placed onto holey carbon-only support films mounted on copper grids.

The Pt dispersion (ratio of surface atoms to total number of atoms) was estimated according to the equation $D = (1.13/d)$, where D is the dispersion and d is the particle size in nm, by assuming spherical particles and a Pt atom density of 1.25×10^{19} atoms/m^2 [65].

The porosity-related properties were determined by measuring N$_2$ adsorption/desorption isotherms at 77 K on a manometric Autosorb-1-MP gas sorption analyzer (Quantachrome). The samples (~50 mg) were previously degassed at 250 °C for 24 h under high vacuum (10^{-6} mbar). Ultra-pure He (99.999%) for void volume calculations and N$_2$ (99.999%) were used. The Brunauer-Emmet-Teller (BET) area values were calculated by following the pertinent consistency criteria (ISO 9277:2010), while the micropore (<2 nm) surface area and volume values were estimated using the carbon black statistical thickness (t-plot) method [66]. The pore size distributions were deduced using the N$_2$-carbon QSDFT (Quenched Solid Density Functional Theory) equilibrium kernel for slit pores [67].

The H$_2$ sorption properties were evaluated up to 20 bar at 77 and 298 K using a PCT Pro-2000 automatic manometric system (SETARAM) equipped with a microdoser module and ultra-pure (99.9999%) H$_2$ gas. A suitable amount of material (~130 mg) was loaded in a stainless steel sample holder and was degassed in-situ after heating to 250 °C, under high vacuum (10^{-7} mbar), for 12 h. Prior to each measurement, the exact volumes of the system were determined via a series of volume calibrations using ultra-pure He (99.999%). Especially for the case of 77 K and in order to avoid He sorption artifacts, dead volumes were calculated by performing volume calculations at 303 K and using a reference curve. Such a curve is constructed by performing several volume calibrations at 303 and 77 K on different quantities of a non-adsorbing material (i.e. non-porous glass). In all cases, the main part of the device remained at constant temperature (i.e. 303 K) with the help of a specially designed air bath. The sample holder was immersed in either a water/ethylene glycol bath (for the measurement at 298 K) or a custom made dewar vessel equipped with a level sensor/auto refill system that ensures negligible temperature variations during the experiments. Simultaneously, kinetic data were recorded for the first dosing step (pressure change from 0 to 2 bar) of three subsequent hydrogenation cycles for the metal-decorated sample. The 1st cycle (full isotherm up to 20 bar) was conducted after the initial evacuation of the sample (at 250 °C for 12 h), the 2nd (only 1 equilibrium point) after completion of the full isotherm and degassing at room temperature overnight and the 3rd (again full isotherm up to 20 bar) after mild heating at 120 °C under high vacuum for 3 h.

The H$_2$ sorption results at 298 K were also used for typical Pt dispersion calculations. The methodology is based on the extrapolation of the amount adsorbed at zero pressure, while it assumes that only surface dissociative chemisorption of hydrogen occurs with a ratio of 1:1 between the sorbed hydrogen atoms and the surface atoms of the Pt particles [68]. The method is in principle straightforward, however, when additional phenomena (e.g. adsorption on the catalyst support, hydride formation and atomic hydrogen spillover) occur the dispersion cannot be calculated. In such cases, according to a previous report [64], the catalyst dispersion obtained from a H$_2$ sorption isotherm can be expressed as pseudo-dispersion (μ), which could be higher than 100%. Moreover, in order to describe the trend of excess hydrogen that spills from a catalyst to the support, the spillover efficiency (η) is defined as the ratio of pseudo-dispersion to catalyst dispersion ($\eta = \mu/D$).

3. Results and discussion

Fig. 2 presents a comparison of the characterization data of the FLG and Pt-FLG materials in terms of XRD, Raman and XPS analysis. The X-ray diffractogram of the FLG powder in Fig. 2a is dominated by the graphitic (002) reflection at 2θ ~26.5°, followed by less-intensive peaks at ~43° and ~54°, which correspond to the (100)/(101) and (004) reflections, respectively (see JCPDS card no. 75−1621). From the peak position of the (002) reflection, the graphene interlayer distance was calculated at ~0.342 nm, which is slightly larger than the equivalent value for graphite (i.e. about 0.334 nm) [69]. The broad peak indicates an estimated domain size of ~4.3 nm based on a FWHM ~2°, using the Scherrer equation, which is about 13 graphene layers per FLG domain. The respective X-ray diffractogram of the Pt-decorated FLG powder (Fig. 2a) reveals similar carbon features with the neat FLG powder, except for the additional Pt (111) and (200) peaks at 2θ ~39° and ~46°, respectively, corresponding to the face centered cubic (FCC) Pt phase (see JCPDS card no. 04−802). The Pt crystal size was calculated from the Pt (111) reflection using the Scherrer equation to ~2.5 nm.

The micro-Raman spectra of the FLG and Pt-FLG powders, shown in Fig. 2b, do not reveal any distinctive spectroscopic differences. Two main broad peaks at 1345 and 1577 cm^{-1} are observed, corresponding to the sp^3 C−C single-bond vibration disorder-induced D-band and the relatively stronger G-band of the sp^2 hybridized carbon, respectively [70]. In addition, a small shoulder of the second higher frequency defect-activated D'-band can be seen at 1612 cm^{-1}. The FWHM of the D, G and D' first order Raman modes is 64, 44 and 40 cm^{-1}, respectively. In the high frequency region, the materials exhibit second order overtones of the D and D' bands, known as the 2D at ~2695 cm^{-1} (with FWHM of 104 cm^{-1}) and the 2D' at ~3230 cm^{-1}, respectively, as well as the combination D + D' defect activated mode at ~2927 cm^{-1}. A weaker broad "shoulder" at 2480 cm^{-1} is also present in both samples. Hence, the Raman spectra are basically identical for both FLG and Pt-FLG samples, thus indicating a retained crystallinity upon Pt decoration. Furthermore, the ratio of the D to G Raman band intensities reflects the percentage of carbon atoms with sp^3 and sp^2 hybridization and is used for the assessment of the disorder in the carbon structure [71,72]. In this respect, the relatively low peak intensity ratio (I_D/I_G = 0.68) and integrated intensity ratio (A_D/A_G = 0.98) as well as the single Lorenzian lineshape of the 2D band verify the high structural quality of the Pt-FLG and FLG samples.

Fig. 2c presents the XPS survey scans of the FLG and Pt-FLG powders. In both cases, in addition to the strong carbon (C 1s) peak, the oxygen (O 1s) peak can be observed, but the nitrogen (N 1s) and platinum peaks (Pt 4f) are very weak and not clearly observable. Table S1 shows the large carbon content (up to ~94.5 at %) for both samples, with the other elements representing less than 6 at%. Using the standard XPS quantification process, the Pt content for the Pt-FLG sample was estimated at ~0.03 at% (or ~0.5 wt%). The high-resolution C 1s, O 1s, N 1s and Pt 4f peaks are presented in
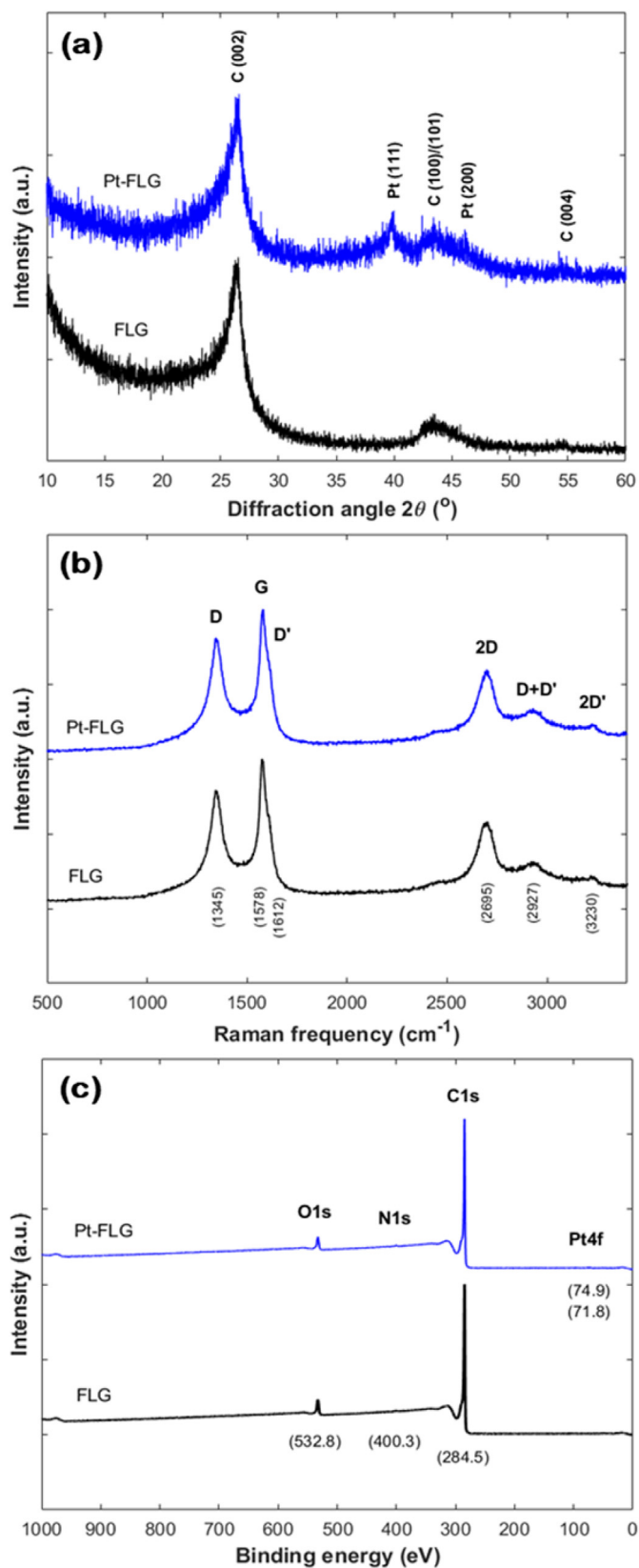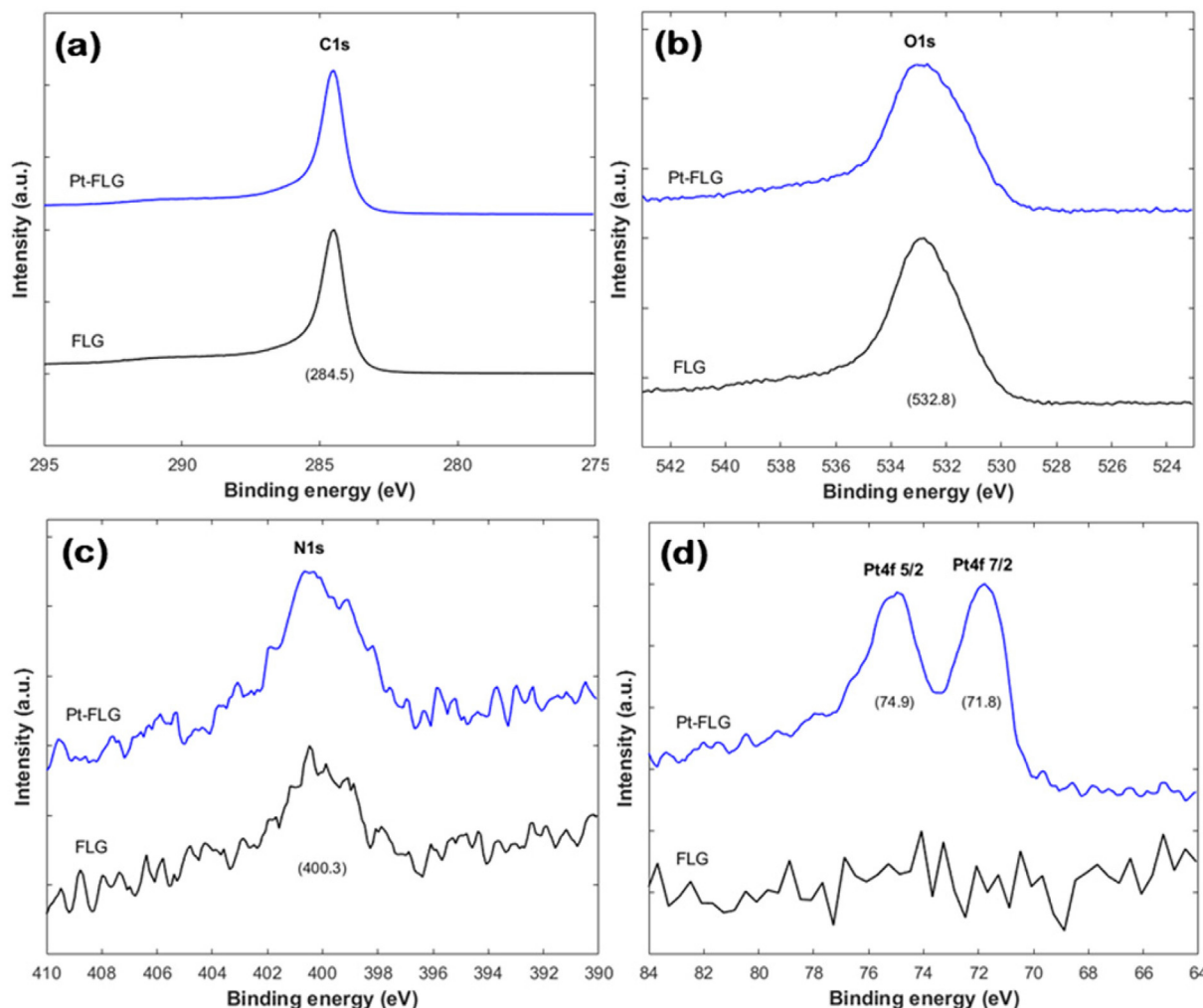
Fig. 2. (a) X-ray diffractograms, (b) micro-Raman spectra and (c) X-ray photoelectron spectra for neat and Pt-decorated FLG powders. (A colour version of this figure can be viewed online.)

Fig. 3. Both FLG and Pt-FLG materials exhibit similar XPS peak shapes for C 1s, O 1s and N 1s. The C 1s spectra (Fig. 3a) demonstrate a strong peak at 284.4 eV, with a peak shape typical of graphite or graphene with probably a small amount of functionalization. The O 1s (Fig. 3b) and N 1s (Fig. 3c) peak maxima occur at 532.8 eV and 400.3 eV, respectively. Their presence indicates the potential existence of oxygen- and nitrogen-based surface functionalities on the FLG surface. The O 1s peak in Fig. 3b is comprised of two components, with the main component located at 532.8 eV and a second component at lower binding energies. Such binding energies are typical of both C—O (high binding energy component at ~533 eV) and C═O/OH⁻ bonding (lower binding energy component at ~531.5 eV) [73], which are all possible surface species on the Pt-FLG sample. If the nitrogen has become incorporated into the FLG structure, then a N 1s peak at ~400.2 eV would most likely be associated with nitrogen directly substituting into the planar carbon six membered ring or as "pyrrolic" nitrogen (i.e. nitrogen in a five-membered ring) [74,75]. Previous work has also shown that a N 1s peak at 400.1 ± 0.2 eV can also arise from the presence of atmospheric contamination, most probably nitrogen-containing organic species [76]. Pt $4f_{7/2}$ and Pt $4f_{5/2}$ peaks at 71.8 eV and 74.9 eV, respectively, can be seen only for the Pt-FLG powder (Fig. 3d). The binding energy of the Pt $4f_{7/2}$ peak (i.e. 71.8 eV) is slightly higher than that expected for Pt metal (71.2 eV), but significantly lower than that expected for Pt oxides. Similar binding energy shifts have been observed several times in Pt-carbon composites and are most probably attributed to the small size of Pt particles [77,78].

Regarding the XPS-determined Pt concentration, the XPS quantification process provides information on the surface (~5 nm) and not the bulk elemental concentrations. There are certain cases where a homogeneous elemental distribution throughout the sample can be assumed (e.g. nitrogen-doped carbons), however, wet chemistry (in contrast to e.g. sputtering) post-synthetic metal doping usually leads to "internalization" of the metal nanoparticles as they are commonly adsorbed within the substrate pores. Thus, the XPS-based Pt concentration (~0.5 wt%) is expected to be significantly lower than the bulk concentration, as determined by using TGA.

The TGA and DSC curves under air flow for the FLG and Pt-FLG powders are combined in Fig. 4. These curves describe the sample mass change (TGA) and the heat flow variation (DSC) as a function of the temperature during the heating process. The original mass of the FLG and Pt-FLG samples decreased by ~10% and ~7%, respectively, upon heating up to ~120 °C, due to desorption of adsorbed moisture and other physisorbed species from their surface. This can be also seen from the endothermic DSC peaks centered at ~120 °C. In both cases, the active mass loss initiates at temperatures above 350 °C. However, the neat FLG is oxidized at a higher temperature compared to the Pt doped FLG, where a rapid mass loss was recorded. This can probably be attributed to the catalytic action of Pt, which may promote carbon oxidation. Above 800 °C a complete "burn-off" was observed for the neat FLG, while there is a residual amount for Pt-FLG pertaining to its metal content. By the end of the heating procedure the residual Pt was ~2 wt %. The equivalent DSC profiles showed an exothermic character up to 800 °C due to decomposition and oxidation phenomena.

The morphological and elemental composition investigations from SEM-EDS and TEM analysis for the Pt-FLG powder are shown in Fig. 5. The irregular chunk-like particle morphology attributed to the initial plasma ablation process, as shown in an FEG SEM image (Fig. 5a), demonstrates no major variation compared to the neat

Fig. 3. High-resolution X-ray photoelectron spectra for the (a) C1s, (b) O1s, (c) N1s and (d) Pt4f orbitals of neat and Pt-decorated FLG powders. (A colour version of this figure can be viewed online.)
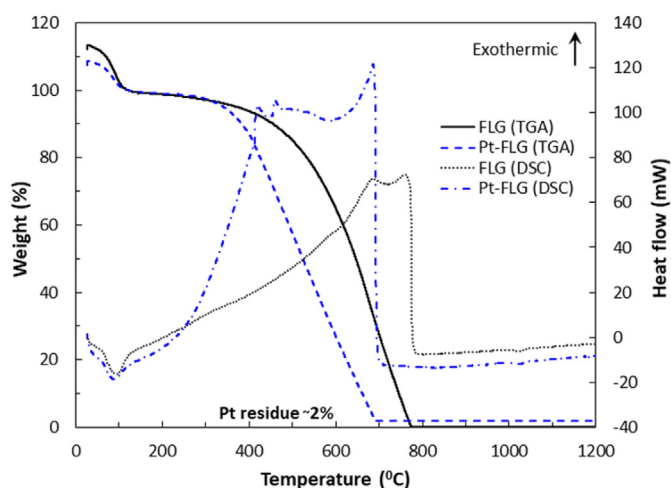

Fig. 4. Combined TGA and DSC curves under synthetic air flow for the neat and Pt-decorated FLG powders. (A colour version of this figure can be viewed online.)

FLG surface [16]. In order to probe the Pt nanoparticles, Fig. 5b shows a BSE image where clear bright dots can be observed on the FLG surface. The BSE images can differentiate chemical contrasts and thus the bright dots are expected to refer to heavy elements such as Pt. The EDS elemental mapping of the Pt-FLG surface revealed that it is mainly composed of carbon (Fig. 5c) along with some oxygen species (Fig. 5d) and, more importantly, confirmed the fact that the previously mentioned bright dots can be assigned to Pt (see Fig. 5e). Finally, well-dispersed Pt nanoparticles through the highly defective FLG surface can be seen in TEM images of lower (Fig. 5f) and higher (Fig. 5g) magnification. In agreement with XRD observations, these nanoparticles exhibit sizes of ~1–2 nm. This is equivalent to a dispersion of 50% or higher based on the equation $D = (1.13/d)$, where D is the dispersion and d is the particle size in nm [65]. A comparison between bright-field and dark-field TEM images for the Pt-FLG material can be found in Fig. S1.

The N_2 adsorption and desorption isotherms recorded at 77 K for the degassed FLG and Pt-FLG powders are displayed in Fig. 6a. It should be noted that for comparison all isotherms and pertinent data have been normalized to pure carbon basis (i.e. by considering a ~2 wt% dead weight due to Pt nanoparticles). Both samples demonstrate a similar trend in their N_2 adsorption/desorption behavior, which suggests that the pore structure is maintained upon Pt decoration. The only difference lies in the adsorbed N_2 volumes, which are a bit higher for the neat FLG case, as can be seen in the inset of Fig. 6a. The increased N_2 volumes at the lower
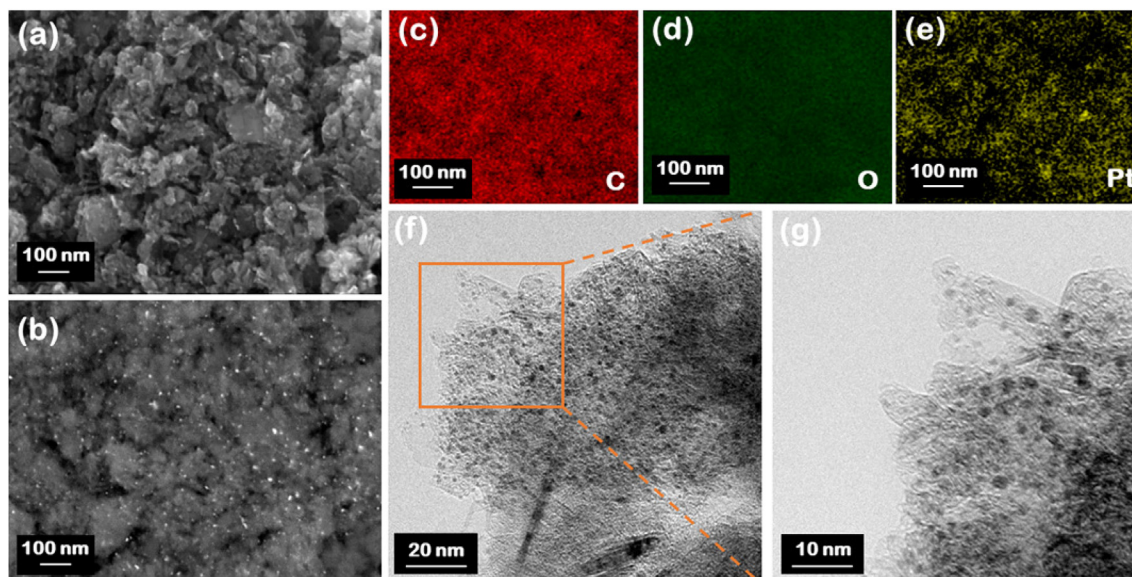
Fig. 5. (a) In-lens field emission gun SEM image (topography contrast) and (b) BSE image (chemical contrast), elemental maps for (c) carbon, (d) oxygen and (e) platinum using EDS and (f) low- and (g) high-magnification TEM images for the Pt-decorated FLG powder. (A colour version of this figure can be viewed online.)

relative pressure regime ($P/P_0 < 0.01$) are attributed to the presence of micropores (i.e. pore widths <2 nm). The formation of a minor hysteresis loop between the adsorption and desorption curves is assigned to capillary N_2 condensation within the mesopores (i.e. pore widths 2–50 nm) [79]. By moving to a close-to-unity relative pressure (P/P_0 ~0.99), the adsorbed N_2 volumes increase in an abrupt manner without reaching a saturation point due to condensation in macropores (i.e. pore widths >50 nm) or adsorption onto external surfaces [80]. Hence, the N_2 isotherms suggest that the FLG and Pt-FLG samples combine microporous, mesoporous and macroporous features.

Table 1 summarizes the porosity-related properties of the degassed FLG and Pt-FLG powders derived by the N_2 data at 77 K. The BET and DFT surface areas of the neat FLG were reduced by less than 10%, upon Pt decoration, while a similar reduction trend was also observed for both the micropore surface area and micropore volume. This could be attributed to a potential limited pore blocking effect due to the deposition of the Pt nanoparticles onto the porous FLG surface [29,30]. The available pores were not significantly "blocked" upon Pt decoration, mainly due to the small size, high degree of dispersion and lack of clustering of the Pt nanoparticles. Fig. 6b shows the pore size distribution curves based on the QSDFT method. Both materials share the same pronounced peak at ~0.7 nm, related to the presence of super-micropores with pore widths between 0.7 and 2 nm, despite the Pt loading. This indicates that the metal deposition does not practically affect the pore size distribution trend. Again, both the differential and cumulative pore volume values (Fig. 6b inset), for this specific pore size, are slightly lower for the Pt-FLG compared to the neat FLG, implying that pore blocking, as expected, occurred only in the narrowest pores of the material.

Fig. 7 presents a collection of H_2 sorption data for the degassed FLG and Pt-FLG powders. High-pressure (0–20 bar) H_2 adsorption and desorption isotherms were recorded at 77 and 298 K (Fig. 7a). All isotherms and pertinent data have been normalized to pure carbon basis, taking into consideration a ~2 wt% dead weight due to Pt nanoparticles, as derived by the TGA method. The excess % gravimetric H_2 uptake values at 20 bar, defined as the percentage of the adsorbed H_2 mass (m_H) and the total system mass (m_H plus

degassed sample mass, m_s); i.e. 100 x $m_H/(m_H + m_s)$, are summarized in Table 1. The H_2 sorption of both samples was fully reversible at 77 K and, while the amounts adsorbed are very similar, the differences in the amounts of adsorbed H_2 are less pronounced compared to N_2 (i.e. a H_2 capacity reduction <5% on pure carbon basis was observed after Pt-decoration). This picture is indeed consistent with limited pore blocking caused by Pt nanoparticles, since exclusion effects should be less important for H_2 due to its significantly smaller molecular size. The amounts adsorbed also come in general agreement with the "Chahine" rule, which states that H_2 physisorption scales with the adsorbent surface area (approximately 1 wt% per 500 m^2/g surface area) [11,18], thus excluding the occurrence of any other phenomena apart from physical adsorption. On the other hand, the H_2 sorption behavior of the Pt-FLG sample at room temperature (298 K) revealed a distinctly different behavior than neat FLG which improved after Pt incorporation. Specifically, the H_2 storage capacity of the Pt-decorated FLG at 20 bar increased by ~56% compared to the neat FLG. Despite the fact that the absolute H_2 uptake value at 298 K for the Pt-FLG is certainly not enough for practical H_2 storage applications, the improvement of the H_2 sorption performance indicates the existence of "weak" H_2 chemisorption phenomena, potentially including the "spillover" effect.

Fig. 7b focuses specifically on the room temperature (298 K) H_2 storage performance of the FLG and Pt-FLG samples. The neat FLG exhibits an almost linear (Henry type) fully reversible sorption behavior, which is typical for H_2 adsorption on carbon surfaces at room temperature, where the Henry constant (i.e. the initial slope of the isotherm) scales with the surface area. This behavior is in contrast to the sudden initial increase of the amount adsorbed as well as the irreversibility exhibited by the Pt-FLG material, both indicating strong deviation from pure physisorption phenomena [55]. In more detail, the abrupt increase of Pt-FLG at lower pressures (<0.5 bar) could be indicative of a possible H_2 chemisorption on the Pt nanoparticles followed by spillover onto the porous FLG support [29,30], while beyond 0.5 bar the picture is qualitatively compatible with physisorption. Nevertheless, even above 0.5 bar sorption is still enhanced as, despite the lower surface area, the uptake curve of Pt-FLG is clearly less linear and its slope (at least
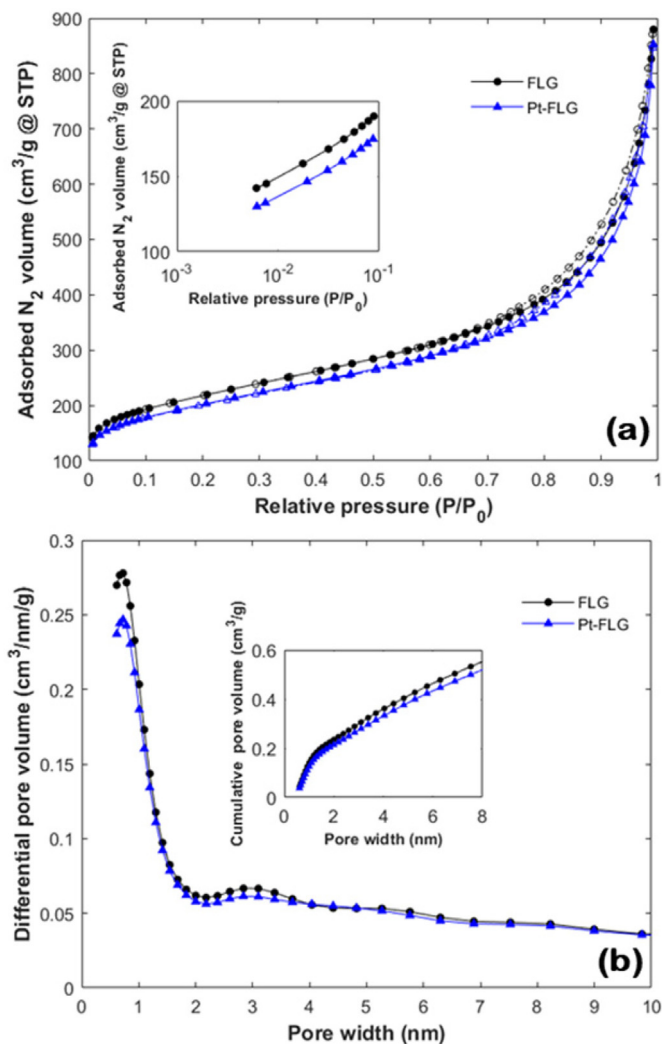
Fig. 6. (a) N_2 adsorption (colored symbols) and desorption (empty symbols) isotherms recorded at 77 K for the neat and Pt-decorated FLG powders; the inset shows the N_2 adsorption behavior at the lower relative pressures ($P/P_0 < 0.1$) using a logarithmic scale and (b) differential pore size distribution based on the QSDFT method for slit pores; the inset shows the cumulative pore size distribution. (A colour version of this figure can be viewed online.)

initially) is higher compared to the neat FLG case. The above observations are consistent with the existence of a second mechanism (apart from physisorption) that has an additive effect on the amount adsorbed. In fact, the shape of the adsorption isotherm implies that this mechanism is strong at lower pressures but gradually loses its significance as the pressure is increased and finally pure adsorption prevails. Indeed, it can be observed that above ~16–17 bar the FLG and Pt-FLG isotherms are almost parallel

to each other (see trendlines in Fig. 7b). In addition, the minor hysteresis between the adsorption and desorption isotherms indicates that the adsorbed H_2 cannot be evacuated by merely pressure reduction.

In order to investigate further the enhanced initial H_2 uptake of the Pt-FLG sample, three sorption-desorption cycles were carried out after following different pre-treatment protocols. The 1st cycle (already described) was conducted after meticulous degassing (i.e. 250 °C/12 h). After measuring the sorption-desorption isotherm the sample was simply evacuated overnight at 25 °C and a single adsorption point was measured (2nd cycle). Consequently, the sample was mildly heated (120 °C) for 3 h under vacuum and another full isotherm was measured (3rd cycle). A first comparison of the amounts adsorbed (first points of the 3 cycles in Fig. 7b) implies that a series of sorption sites were available after the first material activation. However, the solid-fluid interactions are much stronger than Van der Waals forces (physical adsorption forces) in a way that prolonged evacuation at room temperature does not lead to complete desorption and a considerable number of these sites (>50%) are not available in the 2nd cycle. On the other hand, mild heating at 120 °C provides enough activation energy for desorption from these sites and the majority of sorption sites (~80%) are recovered. Overall, the additive effect of weak chemisorption and physisorption at higher pressures leads to a reduction of less than 10% for the 3rd cycle at 20 bar, while the sample reveals a consistent sorption behavior (i.e. similar to the 1st cycle).

An additional support of the weak chemisorption-physisorption combination described above is based on the study of sorption kinetic data. Fig. 7c presents (as fractional uptake versus time) the H_2 sorption kinetics at 298 K for the Pt-FLG sample during three different hydrogenation cycles with a step pressure change from 0 to 2 bar (first equilibrium point of each cycle). In this plot, two markedly different kinetic behaviors have been recorded. The 1st and 3rd cycles show an identical temporal uptake profile that is fully consistent with a relatively slow process, which is consistent with the picture proposed and comprises dissociative H_2 sorption on the surface of Pt particles, spillover of H-atoms to the FLG surface, diffusion of atomic hydrogen to remote sorption sites (e.g. defects) and finally sorption on the site [25,81]. On the other hand, the 2nd cycle exhibits a totally different and much faster process, which can be ascribed to fast sorption on the Pt and FLG surfaces, without significant sorption of spilt over species but apparently a mere dynamic recombination of them followed by desorption. The fast adsorption in the 2nd cycle is also supported by fitting the kinetics in a linear driving force (LDF) model for adsorption rate proportional to vacant sites and a pseudo-second order (PSO) model for strong interaction between adsorbate and sorbent (see Fig. S3) [82]. The PSO model has a better fitting in all three cycles. The rate constants (k) in the PSO model for the 1st and 3rd cycle are almost identical and smaller than the respective k value of the 2nd cycle by a 4.5-fold. Moreover, the LDF model, which describes physisorption behavior, is more applicable in the case of the 2nd cycle (i.e. upon vacuum degassing at room temperature) compared

Table 1
Summary of porosity-related properties and H_2 storage capacities of the degassed FLG and Pt-FLG powders derived from N_2 (77 K) and H_2 (77 and 298 K) sorption data, respectively.
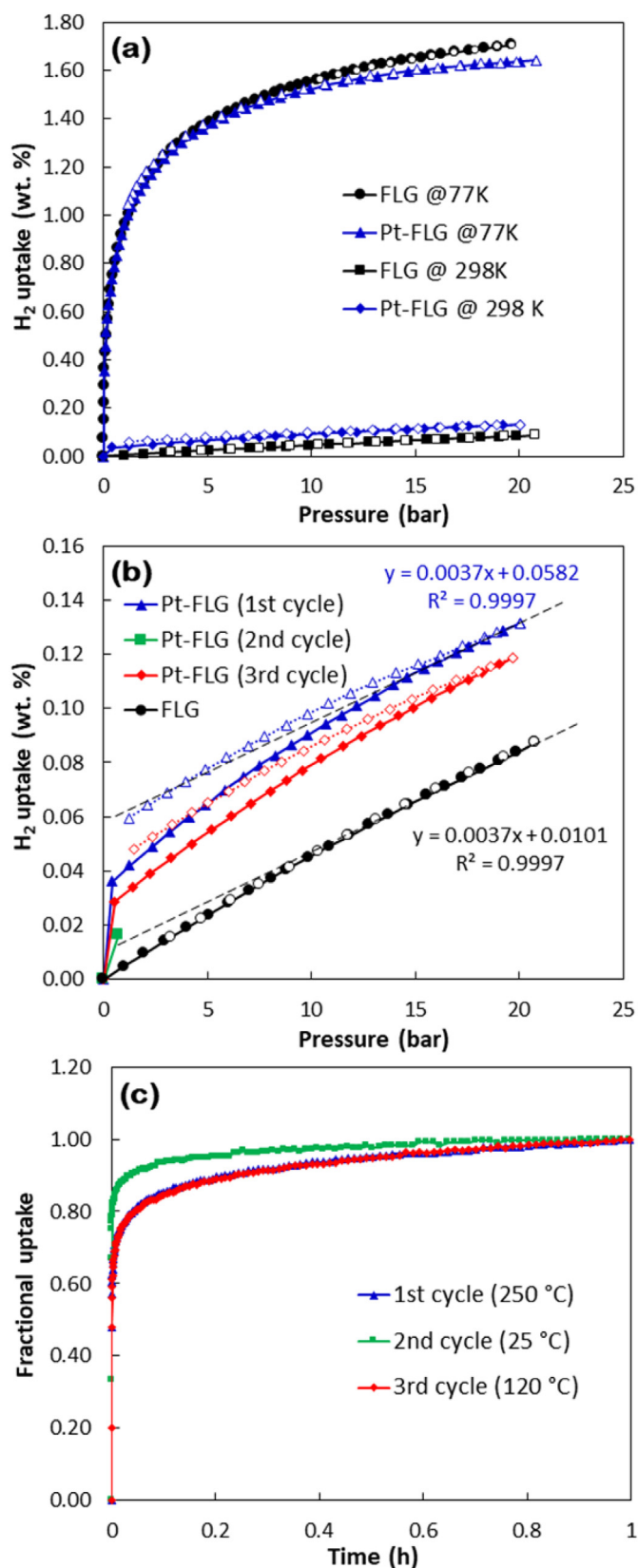
Materials	S_{BET} [m²/g]	S_{DFT} [m²/g]	S_{micro} [m²/g]	V_{micro} [cm³/g]	C_{77K} [wt%]	C_{298K} [wt%]
FLG	776	746	299	0.132	1.71	0.084
Pt-FLG	720	683	261	0.114	1.64	0.131
Relative difference	0.93	0.92	0.87	0.86	0.96	1.56

S_{BET}: Brunauer-Emmett-Teller area, S_{DFT}: cumulative surface area calculated by the Quenched Solid Density Functional Theory (QSDFT) method, S_{micro}: micropore surface area derived by the carbon black statistical thickness (t-plot) method, V_{micro}: micropore volume derived by the t-plot method, C_{77K}: gravimetric H_2 uptake at 77 K and 20 bar, C_{298K}: gravimetric H_2 uptake at 298 K and 20 bar.

Fig. 7. (a) High-pressure (0—20 bar) H₂ adsorption (colored symbols) and desorption (empty symbols) isotherms recorded at 77 and 298 K for the neat and Pt-decorated FLG powders, (b) equivalent H₂ adsorption/desorption behavior (up to 20 bar) focused specifically at room temperature, including three different cycles for the Pt-decorated FLG powder (2nd cycle includes a single adsorption point) and (c) H₂ adsorption kinetics data recorded at 298 K during three different cycles (referring to a

to the other two cycles (i.e. upon vacuum degassing at elevated temperatures). Hence, a high temperature evacuation treatment is necessary for the removal of the remaining H₂, which suggests a possible H₂ chemisorption on the FLG surface. Furthermore, the slow sorption kinetics, when the surface is clean, also supports slow hydrogen radical surface migration after spillover. It should be noted that the adsorption kinetics of the neat FLG (not included here) exhibited a typical physisorption behavior, thus achieving saturation in a matter of seconds.

Since the H₂ uptake step at low pressures indicates dissociative H₂ adsorption on a catalyst surface, it can be used to estimate the metal dispersion [64]. Such calculations relevant to the H₂ sorption isotherm at 298 K of the Pt-FLG material are presented in Tables S2, S3 and S4. For the Pt-FLG case, a pseudo-dispersion of ~340% was calculated for the 1st cycle (see Table S3), while 125 and 260% were calculated for the 2nd and 3rd cycle, respectively. As previously mentioned, a pseudo-dispersion exceeding 100% implies H₂ spill-over. The spillover efficiency (μ), defined as the ratio of pseudo-dispersion to particle dispersion, was up to ~6 for the Pt-FLG case (see Table S3), which is much higher than reported previously for a Pt-activated carbon system (i.e. μ ~1.2) [64]. Hence, the higher the μ value, the more prominent is the spillover effect.

The room temperature H₂ isotherms and kinetics imply H₂ spillover by revealing an improved H₂ uptake, a pseudo-dispersion of more than 100% and a higher sorption isotherm slope. Briefly, the hydrogen molecules (H₂) are dissociated by the Pt nanoparticles into hydrogen atoms (H), the generated H radicals migrate from Pt (Pt—H) by "hopping" over the FLG support and further diffuse on the carbon surface without forming any strong bonds [83]. It has been discussed in the literature that unsaturated bonds on a sorbent surface such as carbon-carbon double/triple bonds [84] as well as surface functionalities such as oxygen [60] may accommodate H radicals. It was also suggested that hydroxyl groups may be formed after H₂ spillover. The C—H and/or O—H interactions are weaker compared to solid chemical bonding but still stronger than Van der Waals forces (i.e. physisorption). This also explains both the observed partial irreversibility during desorption (i.e. small hysteresis) and the slow sorption kinetics. The hysteresis indicates residual hydrogen on the FLG support that cannot be fully removed by a pressure swing. Hydrogen desorption, most probably through recombination, is an activated process (i.e. needs heating) and thus it is associated with a small (yet observable) energy barrier [24]. In terms of kinetics, due to this type of C—H interaction, the slow hydrogen migration on the FLG surface can be observed for hours during the 1st and 3rd cycle, where high temperature treatment was applied prior to H₂ exposure. As only vacuum degassing was applied before the 2nd cycle, saturation was greatly reduced and was reached within minutes, thus implying mainly physisorption.

4. Summary and conclusions

In summary, a plasma-derived nanoporous and high-surface area (~800 m²/g) graphene-based material was decorated with Pt nanoparticles (by thermal reduction under H₂ flow using H₂PtCl₆) towards improving its H₂ storage performance at room temperature via "weak" chemisorption mechanisms (e.g. H₂ spillover). XRD and Raman studies suggested that the graphene structure is properly maintained despite the metal-decoration procedure. XPS analysis showed that the surface chemistry is not affected upon Pt decoration and the nature and concentration of oxygen and nitrogen species has not changed. Combined TGA/DSC analysis revealed

step pressure change from 0 to 2 bar) only for the Pt-decorated FLG powder. (A colour version of this figure can be viewed online.)

that the Pt loading corresponds to ~2 wt%. SEM/EDS and TEM investigations showed well-dispersed (>50%) Pt nanoparticles deposited across the FLG surface with sizes less than 2 nm. N_2 adsorption/desorption data collected at 77 K indicated that Pt-decoration caused no significant alteration of the pore structure and pore size distribution, rather only a 7–8% reduction of the available surface area due to minor pore blocking.

The H_2 sorption properties, including capacity, reversibility and kinetics, were examined under a high-pressure regime (up to 20 bar) both at cryogenic (i.e. 77 K) and room temperature (i.e. 298 K). Even though the Pt presence leads to a "sacrifice" of the cryogenic H_2 uptake, in a similar manner to the surface area reduction trend, the equivalent H_2 storage capacity at room temperature shows an increase by ~56% with respect to the neat FLG material. Such an improvement has been attributed to potential synergetic effects between the porous FLG support and the hosted Pt nanoparticles, including H_2 spillover. The pseudo-dispersion and spillover efficiency were estimated up to ~340% and up to ~6, respectively, indicating a "strong" H_2 spillover behavior. To deal with the partial irreversibility encountered during H_2 desorption, a mild heat treatment under vacuum was applied to remove the residual chemisorbed H_2 and thus regenerate almost completely the Pt-FLG material. The findings of this work provide a crucial understanding of the H_2 storage mechanisms involved in novel platinum group metal-graphene nanocomposite materials.

CRediT authorship contribution statement

Nikolaos Kostoglou: Conceptualization, Methodology, Formal analysis, Investigation, Writing - original draft, Visualization, Project administration. **Chi-Wei Liao:** Investigation. **Cheng-Yu Wang:** Conceptualization, Methodology, Formal analysis, Investigation, Resources, Writing - original draft, Visualization, Supervision, Funding acquisition. **Junko N. Kondo:** Formal analysis, Investigation. **Christos Tampaxis:** Investigation. **Theodore Steriotis:** Conceptualization, Methodology, Formal analysis, Writing - original draft, Visualization, Supervision. **Konstantinos Giannakopoulos:** Investigation, Writing - review & editing. **Athanassios G. Kontos:** Formal analysis, Investigation, Writing - review & editing. **Steve Hinder:** Investigation. **Mark Baker:** Formal analysis, Writing - review & editing, Supervision. **Etienne Bousser:** Investigation. **Allan Matthews:** Writing - review & editing, Supervision. **Claus Rebholz:** Writing - review & editing, Supervision. **Christian Mitterer:** Writing - review & editing, Supervision.

Declaration of competing interest

The authors declare that they have no known competing financial interests or personal relationships that could have appeared to influence the work reported in this paper.

Acknowledgements

Appendix A. Supplementary data

Supplementary data to this article can be found online at https://doi.org/10.1016/j.carbon.2020.08.061.

References

[1] Z. Yang, J. Ren, Z. Zhang, X. Chen, G. Guan, L. Qiu, Y. Zhang, H. Peng, Recent advancement of nanostructured carbon for energy applications, Chem. Rev. 115 (2015) 5159–5223, https://doi.org/10.1021/cr5006217.

[2] L. Schlapbach, A. Züttel, Hydrogen-storage materials for mobile applications, in: Mater. Sustain. Energy A Collect. Peer-Reviewed Res. Rev. Artic. From Nat. Publ. Gr., World Scientific Publishing Co., 2010, pp. 265–270, https://doi.org/10.1142/9789814317665_0038.

[3] H. Reardon, J.M. Hanlon, R.W. Hughes, A. Godula-Jopek, T.K. Mandal, D.H. Gregory, Emerging concepts in solid-state hydrogen storage: the role of nanomaterials design, Energy Environ. Sci. 5 (2012) 5951–5979, https://doi.org/10.1039/c2ee03138h.

[4] J. Ren, N.M. Musyoka, H.W. Langmi, M. Mathe, S. Liao, Current research trends and perspectives on materials-based hydrogen storage solutions: a critical review, Int. J. Hydrogen Energy 42 (2017) 289–311, https://doi.org/10.1016/j.ijhydene.2016.11.195.

[5] A.W.C. Van Den Berg, C.O. Areán, Materials for hydrogen storage: current research trends and perspectives, Chem. Commun. (2008) 668–681, https://doi.org/10.1039/b712576n.

[6] S. McWhorter, K. O'Malley, J. Adams, G. Ordaz, K. Randolph, N.T. Stetson, Moderate temperature dense phase hydrogen storage materials within the US department of energy (DOE) H2 storage program: trends toward future development, Crystals 2 (2012) 413–445, https://doi.org/10.3390/cryst2020413.

[7] DOE technical targets for onboard hydrogen storage for light-duty vehicles | department of energy (n.d.), https://www.energy.gov/eere/fuelcells/doe-technical-targets-onboard-hydrogen-storage-light-duty-vehicles. (Accessed 17 October 2019).

[8] X.B. Zhao, B. Xiao, A.J. Fletcher, K.M. Thomas, Hydrogen adsorption on functionalized nanoporous activated carbons, J. Phys. Chem. B 109 (2005) 8880–8888, https://doi.org/10.1021/jp050080z.

[9] G. Sethia, A. Sayari, Activated carbon with optimum pore size distribution for hydrogen storage, Carbon N. Y. 99 (2016) 289–294, https://doi.org/10.1016/j.carbon.2015.12.032.

[10] N. Kostoglou, C. Koczwara, C. Prehal, V. Terziyska, B. Babic, B. Matovic, G. Constantinides, C. Tampaxis, G. Charalambopoulou, T. Steriotis, S. Hinder, M. Baker, K. Polychronopoulou, C. Doumanidis, O. Paris, C. Mitterer, C. Rebholz, Nanoporous activated carbon cloth as a versatile material for hydrogen adsorption, selective gas separation and electrochemical energy storage, Nanomater. Energy 40 (2017), https://doi.org/10.1016/j.nanoen.2017.07.056.

[11] B. Panella, M. Hirscher, S. Roth, Hydrogen adsorption in different carbon nanostructures, Carbon N. Y. 43 (2005) 2209–2214, https://doi.org/10.1016/j.carbon.2005.03.037.

[12] A. Zolfaghari, P. Pourhossein, H.Z. Jooya, The effect of temperature and topological defects on H2 adsorption on carbon nanotubes, Int. J. Hydrogen Energy 36 (2011) 13250–13254, https://doi.org/10.1016/j.ijhydene.2010.08.086.

[13] K.L. Lim, H. Kazemian, Z. Yaakob, W.R.W. Daud, Solid-state materials and methods for hydrogen storage: a critical review, Chem. Eng. Technol. 33 (2010) 213–226, https://doi.org/10.1002/ceat.200900376.

[14] Y.X. Yang, R.K. Singh, P.A. Webley, Hydrogen adsorption in transition metal carbon nano-structures, Adsorption 14 (2008) 265–274, https://doi.org/10.1007/s10450-007-9089-2.

[15] N. Kostoglou, V. Tzitzios, A.G. Kontos, K. Giannakopoulos, C. Tampaxis, A. Papavasiliou, G. Charalambopoulou, T. Steriotis, Y. Li, K. Liao, K. Polychronopoulou, C. Mitterer, C. Rebholz, Synthesis of nanoporous graphene oxide adsorbents by freeze-drying or microwave radiation: characterization and hydrogen storage properties, Int. J. Hydrogen Energy 40 (2015) 6844–6852, https://doi.org/10.1016/j.ijhydene.2015.03.053.

[16] N. Kostoglou, A. Tarat, I. Walters, V. Ryzhkov, C. Tampaxis, G. Charalambopoulou, T. Steriotis, C. Mitterer, C. Rebholz, Few-layer graphene-like flakes derived by plasma treatment: a potential material for hydrogen adsorption and storage, Microporous Mesoporous Mater. 225 (2016) 482–487, https://doi.org/10.1016/J.MICROMESO.2016.01.027.

[17] V. Jain, B. Kandasubramanian, Functionalized graphene materials for hydrogen storage, J. Mater. Sci. 55 (2020) 1865–1903, https://doi.org/10.1007/s10853-019-04150-y.

[18] R. Chahine, T.K. Bose, Characterization and optimization of adsorbents for hydrogen storage, Hydrog. Energy Prog. 2 (1996) 1259–1264.

[19] D.P. Broom, C.J. Webb, K.E. Hurst, P.A. Parilla, T. Gennett, C.M. Brown,

R. Zacharia, E. Tylianakis, E. Klontzas, G.E. Froudakis, T.A. Steriotis, P.N. Trikalitis, D.L. Anton, B. Hardy, D. Tamburello, C. Corgnale, B.A. van Hassel, D. Cossement, R. Chahine, M. Hirscher, Outlook and challenges for hydrogen storage in nanoporous materials, Appl. Phys. A 122 (2016) 151, https://doi.org/10.1007/s00339-016-9651-4.

[20] R. Chamoun, U.B. Demirci, P. Miele, Cyclic dehydrogenation-(Re)hydrogenation with hydrogen-storage materials: an overview, Energy Technol. 3 (2015) 100–117, https://doi.org/10.1002/ente.201402136.

[21] H.T. Hwang, A. Varma, Hydrogen storage for fuel cell vehicles, Curr. Opin. Chem. Eng. 5 (2014) 42–48, https://doi.org/10.1016/j.coche.2014.04.004.

[22] C.-Y. Wang, C.-W. Chang, Y.-J. Wu, A.D. Lueking, Observation and simulation of hydrogen storage via spillover, Curr. Opin. Chem. Eng. 21 (2018) 116–121, https://doi.org/10.1016/J.COCHE.2018.10.005.

[23] D.S. Pyle, E.M.A. Gray, C.J. Webb, Hydrogen storage in carbon nanostructures via spillover, Int. J. Hydrogen Energy 41 (2016) 19098–19113, https://doi.org/10.1016/j.ijhydene.2016.08.061.

[24] J.H. Guo, S.J. Li, Y. Su, G. Chen, Theoretical study of hydrogen storage by spillover on porous carbon materials, Int. J. Hydrogen Energy (2020), https://doi.org/10.1016/j.ijhydene.2019.12.146.

[25] G.M. Psofogiannakis, G.E. Froudakis, Fundamental studies and perceptions on the spillover mechanism for hydrogen storage, Chem. Commun. 47 (2011) 7933, https://doi.org/10.1039/c1cc11389e.

[26] L. Wang, R.T. Yang, Hydrogen storage on carbon-based adsorbents and storage at ambient temperature by hydrogen spillover, Catal. Rev. 52 (2010) 411–461, https://doi.org/10.1080/01614940.2010.520265.

[27] X. Yu, Z. Tang, D. Sun, L. Ouyang, M. Zhu, Recent advances and remaining challenges of nanostructured materials for hydrogen storage applications, Prog. Mater. Sci. 88 (2017) 1–48, https://doi.org/10.1016/J.PMATSCI.2017.03.001.

[28] T.-Y. Chen, Y. Zhang, L.-C. Hsu, A. Hu, Y. Zhuang, C.-M. Fan, C.-Y. Wang, T.-Y. Chung, C.-S. Tsao, H.-Y. Chuang, Crystal shape controlled H2 storage rate in nanoporous carbon composite with ultra-fine Pt nanoparticle, Sci. Rep. 7 (2017) 42438, https://doi.org/10.1038/srep42438.

[29] D. Giasafaki, G. Charalambopoulou, C. Tampaxis, A. Stubos, T. Steriotis, Hydrogen sorption properties of Pd-doped carbon molecular sieves, Int. J. Hydrogen Energy 39 (2014) 9830–9836, https://doi.org/10.1016/j.ijhydene.2014.02.149.

[30] D. Giasafaki, G. Charalambopoulou, C. Tampaxis, K. Dimos, D. Gournis, A. Stubos, T. Steriotis, Comparing hydrogen sorption in different Pd-doped pristine and surface-modified nanoporous carbons, Carbon N. Y. 98 (2016) 1–14, https://doi.org/10.1016/J.CARBON.2015.10.067.

[31] P.J. Tsai, C.H. Yang, W.C. Hsu, W.T. Tsai, J.K. Chang, Enhancing hydrogen storage on carbon nanotubes via hybrid chemical etching and Pt decoration employing supercritical carbon dioxide fluid, Int. J. Hydrogen Energy 37 (2012) 6714–6720, https://doi.org/10.1016/j.ijhydene.2012.01.032.

[32] C.-H. Chen, T.-Y. Chung, C.-C. Shen, M.-S. Yu, C.-S. Tsao, G.-N. Shi, C.-C. Huang, M.-D. Ger, W.-L. Lee, Hydrogen storage performance in palladium-doped graphene/carbon composites, Int. J. Hydrogen Energy 38 (2013) 3681–3688, https://doi.org/10.1016/J.IJHYDENE.2013.01.070.

[33] H. Zhou, J. Zhang, J. Zhang, X. Yan, X. Shen, A. Yuan, High-capacity room-temperature hydrogen storage of zeolitic imidazolate framework/graphene oxide promoted by platinum metal catalyst, Int. J. Hydrogen Energy 40 (2015) 12275–12285, https://doi.org/10.1016/j.ijhydene.2015.05.199.

[34] H. Zhou, X. Liu, J. Zhang, X. Yan, Y. Liu, A. Yuan, Enhanced room-temperature hydrogen storage capacity in Pt-loaded graphene oxide/HKUST-1 composites, Int. J. Hydrogen Energy 39 (2014) 2160–2167, https://doi.org/10.1016/j.ijhydene.2013.11.109.

[35] Y. Li, R.T. Yang, Hydrogen storage on platinum nanoparticles doped on superactivated carbon, J. Phys. Chem. C 111 (2007) 11086–11094, https://doi.org/10.1021/jp072867q.

[36] N.P. Stadie, J.J. Purewal, C.C. Ahn, B. Fultz, Measurements of hydrogen spillover in platinum doped superactivated carbon, Langmuir 26 (2010) 15481–15485, https://doi.org/10.1021/la9046758.

[37] R. Bhowmick, S. Rajasekaran, D. Friebel, C. Beasley, L. Jiao, H. Ogasawara, H. Dai, B. Clemens, A. Nilsson, Hydrogen spillover in Pt-single-walled carbon nanotube composites: formation of stable C–H bonds, J. Am. Chem. Soc. 133 (2011) 5580–5586, https://doi.org/10.1021/ja200403m.

[38] J.L. Blackburn, C. Engtrakul, J.B. Bult, K. Hurst, Y. Zhao, Q. Xu, P.A. Parilla, L.J. Simpson, J.D.R. Rocha, M.R. Hudson, C.M. Brown, T. Gennett, Spectroscopic identification of hydrogen spillover species in ruthenium-modified high surface area carbons by diffuse reflectance infrared Fourier transform spectroscopy, J. Phys. Chem. C 116 (2012) 26744–26755, https://doi.org/10.1021/jp305235p.

[39] X.M. Liu, Y. Tang, E.S. Xu, T.C. Fitzgibbons, G.S. Larsen, H.R. Gutierrez, H.H. Tseng, M.S. Yu, C.S. Tsao, J.V. Badding, V.H. Crespi, A.D. Lueking, Evidence for ambient-temperature reversible catalytic hydrogenation in Pt-doped carbons, Nano Lett. 13 (2013) 137–141, https://doi.org/10.1021/nl303673z.

[40] C.-S. Tsao, Y. Liu, M. Li, Y. Zhang, J.B. Leao, H.-W. Chang, M.-S. Yu, S.-H. Chen, Neutron scattering methodology for absolute measurement of room-temperature hydrogen storage capacity and evidence for spillover effect in a Pt-doped activated carbon, J. Phys. Chem. Lett. 1 (2010) 1569–1573, https://doi.org/10.1021/jz1004472.

[41] C.S. Tsao, Y. Liu, H.Y. Chuang, H.H. Tseng, T.Y. Chen, C.H. Chen, M.S. Yu, Q. Li, A. Lueking, S.H. Chen, Hydrogen spillover effect of pt-doped activated carbon studied by inelastic neutron scattering, J. Phys. Chem. Lett. 2 (2011) 2322–2325, https://doi.org/10.1021/jz2010368.

[42] Y. Liu, C.M. Brown, D.A. Neumann, D.B. Geohegan, A.A. Puretzky, C.M. Rouleau, H. Hu, D. Styers-Barnett, P.O. Krasnov, B.I. Yakobson, Metal-assisted hydrogen storage on Pt-decorated single-walled carbon nanohorns, Carbon N. Y. 50 (2012) 4953–4964, https://doi.org/10.1016/J.CARBON.2012.06.028.

[43] Z. Geng, D. Wang, C. Zhang, X. Zhou, H. Xin, X. Liu, M. Cai, Spillover enhanced hydrogen uptake of Pt/Pd doped corncob-derived activated carbon with ultra-high surface area at high pressure, Int. J. Hydrogen Energy 39 (2014) 13643–13649, https://doi.org/10.1016/J.IJHYDENE.2014.02.065.

[44] R. Zacharia, S. Rather, S.W. Hwang, K.S. Nahm, Spillover of physisorbed hydrogen from sputter-deposited arrays of platinum nanoparticles to multi-walled carbon nanotubes, Chem. Phys. Lett. 434 (2007) 286–291, https://doi.org/10.1016/J.CPLETT.2006.12.022.

[45] C.S. Tsao, Y.R. Tzeng, M.S. Yu, C.Y. Wang, H.H. Tseng, T.Y. Chung, H.C. Wu, T. Yamamoto, K. Kaneko, S.H. Chen, Effect of catalyst size on hydrogen storage capacity of Pt-impregnated active carbon via spillover, J. Phys. Chem. Lett. 1 (2010) 1060–1063, https://doi.org/10.1021/jz100149u.

[46] A.A.S. Nair, R. Sundara, N. Anitha, Hydrogen storage performance of palladium nanoparticles decorated graphitic carbon nitride, Int. J. Hydrogen Energy 40 (2015) 3259–3267, https://doi.org/10.1016/j.ijhydene.2014.12.065.

[47] N.R. Stuckert, L. Wang, R.T. Yang, Characteristics of hydrogen storage by spillover on Pt-doped carbon and catalyst-bridged metal organic framework, Langmuir 26 (2010) 11963–11971, https://doi.org/10.1021/la101377u.

[48] Y. Jeong, T.C.M. Chung, Mono-dispersed transition metal nanoparticles on boron-substituted carbon support and applications in hydrogen storage, Carbon N. Y. 49 (2011) 140–146, https://doi.org/10.1016/j.carbon.2010.08.053.

[49] P. Kundu, C. Nethravathi, P.A. Deshpande, M. Rajamathi, G. Madras, N. Ravishankar, Ultrafast microwave-assisted route to surfactant-free ultra-fine Pt nanoparticles on graphene: synergistic co-reduction mechanism and high catalytic activity, Chem. Mater. 23 (2011) 2772–2780, https://doi.org/10.1021/cm200329a.

[50] P. Jain, D.A. Fonseca, E. Schaible, A.D. Lucking, Hydrogen uptake of platinum-doped graphite nanofibers and stochastic analysis of hydrogen spillover, J. Phys. Chem. C 111 (2007) 1788–1800, https://doi.org/10.1021/jp0654922.

[51] L. Wang, R.T. Yang, New sorbents for hydrogen storage by hydrogen spillover – a review, Energy Environ. Sci. 1 (2008) 268, https://doi.org/10.1039/b807957a.

[52] H. Chen, L. Wang, J. Yang, R.T. Yang, Investigation on hydrogenation of metal-organic frameworks HKUST-1, MIL-53, and ZIF-8 by hydrogen spillover, J. Phys. Chem. C 117 (2013) 7565–7576, https://doi.org/10.1021/jp401367k.

[53] C.-H. Chen, C.-C. Huang, Effect of surface characteristics and catalyst loaded amount on hydrogen storage in carbon nanotubes, Microporous Mesoporous Mater. 112 (2008) 553–560, https://doi.org/10.1016/J.MICROMESO.2007.10.038.

[54] Y. Suttisawat, P. Rangsunvigit, B. Kitiyanan, M. Williams, P. Ndungu, M.V. Lototskyy, A. Nechaev, V. Linkov, S. Kulprathipanja, Investigation of hydrogen storage capacity of multi-walled carbon nanotubes deposited with Pd or V, Int. J. Hydrogen Energy 34 (2009) 6669–6675, https://doi.org/10.1016/j.ijhydene.2009.06.063.

[55] H. Nishihara, T. Simura, T. Kyotani, Enhanced hydrogen spillover to fullerene at ambient temperature, Chem. Commun. 54 (2018) 3327–3330, https://doi.org/10.1039/c8cc00265g.

[56] W. Karim, C. Spreafico, A. Kleibert, J. Gobrecht, J. VandeVondele, Y. Ekinci, J.A. van Bokhoven, Catalyst support effects on hydrogen spillover, Nature 541 (2017) 68–71, https://doi.org/10.1038/nature20782.

[57] S. Nachimuthu, P.J. Lai, J.C. Jiang, Efficient hydrogen storage in boron doped graphene decorated by transition metals - a first-principles study, Carbon N. Y. 73 (2014) 132–140, https://doi.org/10.1016/j.carbon.2014.02.048.

[58] L. Wang, F.H. Yang, R.T. Yang, M.A. Miller, Effect of surface oxygen groups in carbons on hydrogen storage by spillover, Ind. Eng. Chem. Res. 48 (2009) 2920–2926, https://doi.org/10.1021/ie8014507.

[59] E. Díaz, M. León, S. Ordóñez, Hydrogen adsorption on Pd-modified carbon nanofibres: influence of CNF surface chemistry and impregnation procedure, Int. J. Hydrogen Energy 35 (2010) 4576–4581, https://doi.org/10.1016/j.ijhydene.2010.02.119.

[60] Q. Li, A.D. Lueking, Effect of surface oxygen groups and water on hydrogen spillover in Pt-doped activated carbon, J. Phys. Chem. C 115 (2011) 4273–4282, https://doi.org/10.1021/jp105923a.

[61] T.-Y. Chung, C.-S. Tsao, H.-P. Tseng, C.-H. Chen, M.-S. Yu, Effects of oxygen functional groups on the enhancement of the hydrogen spillover of Pd-doped activated carbon, J. Colloid Interface Sci. 441 (2015) 98–105, https://doi.org/10.1016/J.JCIS.2014.10.062.

[62] G. Zhao, D. Shao, C. Chen, X. Wang, Synthesis of few-layered graphene by H2 O2 plasma etching of graphite, Appl. Phys. Lett. 98 (2011) 183114, https://doi.org/10.1063/1.3589354.

[63] N. McEvoy, H. Nolan, N. Ashok Kumar, T. Hallam, G.S. Duesberg, Functionalisation of graphene surfaces with downstream plasma treatments, Carbon N. Y. 54 (2013) 283–290, https://doi.org/10.1016/J.CARBON.2012.11.040.

[64] C.-Y. Wang, Q. Gong, Y. Zhao, J. Li, A.D. Lueking, Stability and hydrogen adsorption of metal–organic frameworks prepared via different catalyst doping methods, J. Catal. 318 (2014) 128–142, https://doi.org/10.1016/J.JCAT.2014.07.010.

[65] R.M. Rioux, H. Song, J.D. Hoefelmeyer, P. Yang, G.A. Somorjai, High-surface-area catalyst design: synthesis, characterization, and reaction studies of platinum nanoparticles in mesoporous SBA-15 silica, J. Phys. Chem. B 109 (2005) 2192–2202, https://doi.org/10.1021/jp048867x.

[66] J.H. de Boer, B.G. Linsen, T. van der Plas, G.J. Zondervan, Studies on pore systems in catalysts. VII. Description of the pore dimensions of carbon blacks by the t method, J. Catal. 4 (1965) 649–653, https://doi.org/10.1016/0021-9517(65)90264-2.

[67] A.V. Neimark, Y. Lin, P.I. Ravikovitch, M. Thommes, Quenched solid density functional theory and pore size analysis of micro-mesoporous carbons, Carbon N. Y. 47 (2009) 1617–1628, https://doi.org/10.1016/j.carbon.2009.01.050.

[68] L. Spenadel, M. Boudart, Dispersion of platinum on supported catalysts, J. Phys. Chem. 64 (1960) 204–207, https://doi.org/10.1021/j100831a004.

[69] D.D.L. Chung, Review: graphite, J. Mater. Sci. 37 (2002) 1475–1489, https://doi.org/10.1023/A:1014915307738.

[70] Z. Ni, Y. Wang, T. Yu, Z. Shen, Raman spectroscopy and imaging of graphene, Nano Res 1 (2008) 273–291, https://doi.org/10.1007/s12274-008-8036-1.

[71] Z. Sun, X. Huang, F. Liu, X. Yang, C. Rösler, R.A. Fischer, M. Muhler, W. Schuhmann, Amine-based solvents for exfoliating graphite to graphene outperform the dispersing capacity of N-methyl-pyrrolidone and surfactants, Chem. Commun. 50 (2014) 10382–10385, https://doi.org/10.1039/c4cc03923h.

[72] Z. Sun, J. Masa, P. Weide, S.M. Fairclough, A.W. Robertson, P. Ebbinghaus, J.H. Warner, S.C.E. Tsang, M. Muhler, W. Schuhmann, High-quality functionalized few-layer graphene: facile fabrication and doping with nitrogen as a metal-free catalyst for the oxygen reduction reaction, J. Mater. Chem. A. 3 (2015) 15444–15450, https://doi.org/10.1039/c5ta02248g.

[73] M. Peuckert, H.P. Bonzel, Characterization of oxidized platinum surfaces by X-ray photoelectron spectroscopy, Surf. Sci. 145 (1984) 239–259, https://doi.org/10.1016/0039-6028(84)90778-7.

[74] M. Scardamaglia, B. Aleman, M. Amati, C. Ewels, P. Pochet, N. Reckinger, J.F. Colomer, T. Skaltsas, N. Tagmatarchis, R. Snyders, L. Gregoratti, C. Bittencourt, Nitrogen implantation of suspended graphene flakes: annealing effects and selectivity of sp2 nitrogen species, Carbon N. Y. 73 (2014) 371–381, https://doi.org/10.1016/j.carbon.2014.02.078.

[75] T. Susi, T. Pichler, P. Ayala, X-ray photoelectron spectroscopy of graphitic carbon nanomaterials doped with heteroatoms, Beilstein J. Nanotechnol. 6 (2015) 177–192, https://doi.org/10.3762/bjnano.6.17.

[76] M.A. Baker, H. Fakhouri, R. Grilli, J. Pulpytel, W. Smith, F. Arefi-Khonsari, Effect of total gas pressure and O2/N2 flow rate on the nanostructure of N-doped TiO2 thin films deposited by reactive sputtering, Thin Solid Films 552 (2014) 10–17.

[77] M.G. Mason, Electronic structure of supported small metal clusters, Phys. Rev. B 27 (1983) 748–762, https://doi.org/10.1103/PhysRevB.27.748.

[78] Z. Bayindir, P.N. Duchesne, S.C. Cook, M.A. MacDonald, P. Zhang, X-ray spectroscopy studies on the surface structural characteristics and electronic properties of platinum nanoparticles, J. Chem. Phys. 131 (2009) 244716, https://doi.org/10.1063/1.3276917.

[79] M. Thommes, K. Kaneko, A.V. Neimark, J.P. Olivier, F. Rodriguez-Reinoso, J. Rouquerol, K.S.W. Sing, Physisorption of gases, with special reference to the evaluation of surface area and pore size distribution (IUPAC Technical Report), Pure Appl. Chem. 87 (2015) 1051–1069, https://doi.org/10.1515/pac-2014-1117.

[80] N. Kostoglou, V. Ryzhkov, I. Walters, C. Doumanidis, C. Rebholz, C. Mitterer, Arc-produced short-length multi-walled carbon nanotubes as "millstones" for the preparation of graphene-like nanoplatelets, Carbon N. Y. (2019), https://doi.org/10.1016/j.carbon.2019.02.054.

[81] C.H. Chen, M.S. Yu, C.S. Tsao, H.Y. Chuang, H.H. Tseng, T.Y. Chung, Characterization of hydrogen adsorption in platinum-doped microporous carbon with varied catalytic properties, Microporous Mesoporous Mater. 152 (2012) 157–162, https://doi.org/10.1016/j.micromeso.2011.11.041.

[82] C.W. Chang, Y.H. Kao, P.H. Shen, P.C. Kang, C.Y. Wang, Nanoconfinement of metal oxide MgO and ZnO in zeolitic imidazolate framework ZIF-8 for CO2 adsorption and regeneration, J. Hazard Mater. 400 (2020) 122974, https://doi.org/10.1016/j.jhazmat.2020.122974.

[83] R. Osuga, T. Yokoi, K. Doitomi, H. Hirao, J.N. Kondo, Infrared investigation of dynamic behavior of brønsted acid sites on zeolites at high temperatures, J. Phys. Chem. C 121 (2017) 25411–25420, https://doi.org/10.1021/acs.jpcc.7b09846.

[84] H. Cheng, L. Chen, A.C. Cooper, X. Sha, G.P. Pez, Hydrogen spillover in the context of hydrogen storage using solid-state materials, Energy Environ. Sci. 1 (2008) 338–354, https://doi.org/10.1039/b807618a.